

---

**This manuscript is a preprint** and has not undergone peer-review. Subsequent versions of this manuscript may have different content. If accepted, the final version of this manuscript will be available via the '*Peer-reviewed Publication DOI*' link on the right-hand side of this webpage. Please feel free to contact any of the authors directly or to comment on the manuscript using **hypothes.is** (<https://web.hypothes.is/>). We welcome feedback!

---

# The formation and implications of giant blocks and fluid escape structures in submarine lateral spreads

Nan Wu<sup>1</sup>, Christopher A-L. Jackson<sup>1</sup>, Howard D. Johnson<sup>1</sup>, David M. Hodgson<sup>2</sup>, Michael A. Clare<sup>3</sup>,  
Harya D. Nugraha<sup>1</sup>, Wei Li<sup>4</sup>

<sup>1</sup>Basins Research Group (BRG), Department of Earth Science & Engineering, Imperial College, Prince Consort Road, London, SW7 2BP, UK

<sup>2</sup>School of Earth and Environment, University of Leeds, Leeds, LS2 9JT, UK

<sup>3</sup>National Oceanography Centre, Southampton SO14 3ZH, UK

<sup>4</sup>South China Sea Institute of Oceanology, Chinese Academy of Sciences, China

## Abstract

Lateral spread (or ‘spreading’) and submarine creep are processes that occur near the headwalls of both terrestrial landslides and submarine mass-transport complexes (MTCs). Both submarine creep and spread deposits may contain giant (km-scale) coherent blocks, but their transport processes remain poorly constrained. Here we use 2D and 3D seismic reflection data to determine the geometry, scale, and origin of an ancient (Late Miocene) mass-transport complex (MTC) located in the Kangaroo Syncline, offshore NW Australia. We show that this large remobilised mass of carbonate ooze is c. 170-300 m thick and covers an area of at least c. 1050 km<sup>2</sup>. The deposit is defined internally by two distinct seismic facies: (i) large, upward-tapering blocks (up to 210-300 m thick, 170-210 m wide, and 800-1200 m long) with negligible internal deformation, which decrease in height and spacing along the transport direction (identical, but *in situ*, seismic facies forms undeformed slope material immediately updip of the deposit headwall); and (ii) troughs (160-260 m thick, 190-230 m wide and 800-1200 m long) comprising moderately deformed strata, which contain ‘v’-shaped, pipe-like structures that extend upwards from the inferred basal shear surface to the top surface of the MTC. The lack of deformation within the blocks, and their correlation to adjacent in-situ deposits, suggests they underwent very limited transport (c. 50 m-70 m). The relatively high degree of deformation within the intervening troughs is attributed to the vertical expulsion of fluids and sediment during hydraulic failure of the sediment mass. We present a hydraulic failure model that accounts for the styles and patterns of intra-MTC

30 deformation process. This model invokes evacuation of the lower slope by a pre-cursor MTC  
31 that formed the space to trigger the lateral spread event. Our study provides new insights  
32 into the genesis and rheology of subaqueous lateral spreads, enabling improved assessments  
33 of the threats posed to critical seafloor infrastructure. The genetic links identified between  
34 mass wasting and spatially-focused fluid flow indicate that, as well as disturbing the deep  
35 seafloor, submarine landslides may also create important deep-sea biodiversity hotspots.

36 Keywords: spread, slope failure, geohazard, mass-transport complex (MTC), submarine  
37 landslide, Exmouth Plateau, NW Shelf, Australia

## 38 Introduction

39 Mass-transport complex (MTC) is a broad term typically used to describe slope failure  
40 deposits resulting from creep, spread, slide, slump, and debris flow processes (Figure 1;  
41 Nemec, 1990; Varnes, 1978). MTCs are responsible for transporting large volumes of  
42 sediments from basin margins to the adjacent basin floor, often during single catastrophic  
43 events (e.g. Posamentier and Martinsen, 2011). Because of their size, the generation and  
44 emplacement of MTCs play a key role in shaping and controlling the stratigraphic evolution  
45 of continental margins around the world (Posamentier and Martinsen, 2011). MTCs can  
46 initiate and translate over very low-angle seafloors by hydroplaning, with sediments in the  
47 overlying failure mass partly or fully disaggregated to form a genetically related debris flow  
48 (De Blasio and Elverhoi, 2011). Partial disaggregation can result in the formation and  
49 emplacement of relatively coherent, largely undeformed blocks (Alves, 2015; Jackson, 2011;  
50 Li et al., 2016; Micallef et al., 2007) that may trigger tsunamis (Tappin, 2010), could damage  
51 or destroy seabed infrastructure (Masson et al., 2006; Urlaub et al., 2013), be a pre-cursor for  
52 subsequent slope failure events (i.e. Lee and Chough, 2001; Li et al., 2016), or increase the  
53 slope stability by reducing gravitational potential (Shillington et al., 2012). The nature of any  
54 impacts to seafloor structures, and also the potential for tsunamigenesis, strongly depend on  
55 the degree of landslide disaggregation, the volume and strength of the failed mass, its  
56 mobility, speed and direction of movement (e.g. Dutta and Hawlader, 2019; Randolph and  
57 White, 2012; Watts et al., 2005; Zakeri, 2009; Zhu and Randolph, 2010). For instance, highly  
58 mobile, yet relatively thin debris flows have toppled oil and gas platforms, and ruptured  
59 pipelines in the Gulf of Mexico (e.g. Chaytor et al., 2020). Conversely, much larger, deep-  
60 seated (i.e. relatively thick), and yet limited run-out MTCs triggered by the 2011 Tōhoku-Oki

61 earthquake ( $M_w$  9.1) caused no discernable damage to seafloor telecommunication cables  
62 (e.g. Pope et al., 2017; Strasser et al., 2013). Therefore, differentiating the nature of slope  
63 failure processes is a key element in assessing their risk to coastal communities and critical  
64 seafloor infrastructure.

65 Submarine creep (or 'spreading') and lateral spreading are gravity-driven processes that occur  
66 near the headwall area of sediment failure in marine (syn.: 'submarine spread') and terrestrial  
67 (landslides) settings, respectively (Figure 1). Submarine creep is defined as a slow, gravity-  
68 driven, downslope motion or post- or syn-depositional deformation of a sediment mass  
69 (Nemec, 1990; Silva and Booth, 1984). The deposits of submarine creep may contain giant  
70 coherent blocks that are up to c. 300 m high and c. 4 km wide (e.g. Li et al., 2016).

71 Subaqueous spread (also known as gravitational spreading and lateral spreading; Savage and  
72 Varnes, 1987; Varnes, 1978) is another type of gravity-induced failure. First defined in  
73 terrestrial settings as 'lateral spreading', this type of failure is triggered by subsurface  
74 liquefaction and the formation of an intra-stratal weak zone, above which the failed mass  
75 translates (Varnes, 1978). Commonly, these masses are stretched and broken up into  
76 internally coherent blocks (Figure 1). A key characteristics of spreads is that they can occur  
77 above a very gently-dipping (*ca.*  $< 1^\circ$ ) failure surface (Cruden and Varnes, 1996; Micallef et al.,  
78 2007). A subaqueous spread can have a lateral displacement of only a few tens of metres  
79 (Micallef et al., 2007). Despite this, onshore analogues indicate that the emplacement of  
80 spread-related blocks could be extremely hazardous. For example, a spread and its associated  
81 debris occurred in Palu, Indonesia, following an earthquake in September 2018, leaving >2000  
82 people dead and c. 1300 people missing (Bradley et al., 2019; Watkinson and Hall, 2019).  
83 Subaqueous spread-related deposits have received less attention than their terrestrial  
84 counterparts, despite 3D seismic reflection data being an excellent tool to resolve the external  
85 and internal geometry, and origin of this particular type of submarine landslide (Micallef et  
86 al., 2007). Although the deposits of submarine creep and spread have similar external  
87 geometries and internal seismic facies, they are different failure process and are typically not  
88 considered part of a continuum; i.e. creep would not transform into spread, or vice versa.

89 Many landslide hazard assessments are based solely on plan-view imaging using multibeam  
90 bathymetric surveys (e.g. Geertsema et al., 2018). While incredibly valuable, such surveys the  
91 lack subsurface information required to identify and diagnose the style and depth of landslide

92 failure, and the nature of internal deformation. Here we demonstrate the value of high  
93 resolution 2D and 3D seismic reflection data to complement and advance modern seafloor  
94 studies of MTCs. Our aim is to evaluate the morphology, internal structure, kinematics, origin  
95 and geohazard risk of a large submarine MTC using a high-quality, 3D and 2D seismic  
96 reflection dataset from the NW Shelf, offshore Australia. Using these data, we can quantify  
97 the height and spacing of the contained blocks, whereas a detailed kinematic analysis of intra-  
98 MTC structures allows the transport direction to be determined. The study also aims to offer  
99 a better understanding of spread initiation, translation, and deposition, which will help to  
100 build a more comprehensive model for submarine mass failures and to help understand, and  
101 hence inform mitigation of the associated geohazard risk.

## 102 **Geological setting**

103 The Exmouth Plateau is located offshore NW Australia, c. 900 km south of the tectonically-  
104 active boundary between the Australian and Eurasian tectonic plates (Fig. 2a, 2b) (Hengesh  
105 et al., 2013; Hengesh et al., 2012). The Exmouth Plateau is c. 600 km long and c. 350 km wide,  
106 and is presently located in water depths of 1100-5000 m (Exon et al., 1992; Falvey and Veevers,  
107 1974; Hengesh et al., 2013) (Figure 2a). This study focuses on the Upper Miocene to Holocene  
108 passive margin mega-sequence (Figure 2c). This interval records the relatively slow deposition  
109 (c. 0.02 mm/yr) of very fine-grained carbonate in bathyal (200-2000 m) water depths (Exon  
110 et al., 1992; Haq et al., 1992; Maher and Thompson, 1999). Cores from Ocean Drilling Program  
111 (ODP) wells 762 and 763 have established that the dominant lithology in this interval is  
112 nannofossil-rich carbonate ooze (Boyd et al., 1993; Exon et al., 1992; Haq et al., 1992). These  
113 deposits are characterised by high porosities (c. 70%) and high water saturations (c. 40%), and  
114 by an overall low strength profile (<20kPa) (see Figure 5 from Hengesh et al., 2012; von Rad,  
115 1992). These physical properties increase the slope instability and related geohazard risk of  
116 the Exmouth Plateau area. Prolonged slope instability is recorded in the presence of large  
117 (e.g. c. 500km<sup>3</sup> gorgon slide; Hengesh et al., 2012), stacked, slope-to-basin floor MTCs in the  
118 upper part (i.e. post-Oligocene) of the passive margin mega-sequence (Hengesh et al., 2012;  
119 Nugraha et al., 2019; Nugraha et al., 2018; Scarselli et al., 2013). The study area is located in  
120 the axis of the Kangaroo Syncline, between the Exmouth Plateau to the west and the NW  
121 Shelf to the east (Figure 2a, 2d). The stratigraphic interval under investigation extends  
122 upwards from Horizon H1 (base) to the seabed (top) (Figure 2c, 3a-c). Horizon H1 (Figure 3b)

123 is a regionally mappable unconformity that defines the base of the Late Miocene, and which  
124 records collision of the Australian and Eurasian plates (Boyd et al., 1993; Hull and Griffiths,  
125 2002). The Late Miocene to Holocene succession thickens basinwards into the axis of the  
126 Kangaroo Syncline, and thins to the east and west, towards the NW Shelf and the crest of  
127 Exmouth Plateau, respectively (Nugraha et al., 2018).

## 128 Dataset and Methodology

129 In this study we use two types of seismic reflection data provided by Geoscience Australia  
130 (<http://www.ga.gov.au/nopims>): (i) up to c. 500 km long, 2D seismic reflection surveys, which  
131 were collected between 1993 and 2005; and (ii) a 3D seismic reflection survey (Willem 3D  
132 seismic survey), which was acquired by Veritas DGC Australia in 2006. The Willem 3D seismic  
133 survey covers a total area of c. 2628 km<sup>2</sup>, extending along the Exmouth continental slope and  
134 across the lower slope into the Kangaroo Syncline (Figure 2a-b). A downward decrease and  
135 increase in acoustic impedance are expressed as blue (negative) and red (positive) reflection  
136 events, respectively (Figure 3a). We estimate the spatial resolution of the Willem seismic  
137 survey using the frequency content (c. 60 Hz decreasing to c. 40 Hz) and average seismic  
138 velocity (1500 m/s decreasing to 2000 m/s) between the seabed and H1. Based on these data,  
139 we calculate an approximate spatial resolution of 6.25 m at the seabed, decreasing to 11 m  
140 near the base of the studied interval. This imaging quality is sufficient to map, at relatively  
141 high-resolution, the geometry of structural features (e.g. scours, faults, etc) immediately  
142 below and within the studied MTC.

143 We adopt the seismic-stratigraphic framework of Nugraha et al. (2018), which is based on  
144 their analysis of the Exmouth Plateau, c. 50 km SW of the study area (Figure 2a). Our study  
145 interval falls within SU3 of Nugraha et al. (2018), within which we map four horizons based  
146 on the seismic continuity, amplitude, and frequency/spacing, as well as the seismic facies  
147 characteristics of the packages they bound. The lithology and geotechnical properties (i.e.  
148 water content, porosity, shear strength, etc.) of the studied stratigraphic interval are inferred  
149 from ODP Wells 762 and 763, which are located c. 300 km SW of the study area where they  
150 penetrate a similar seismic-stratigraphic succession. We extracted seismic attributes, such as  
151 variance and amplitude contrast (see Supporting Information Appendix 1 for explanation),  
152 from the 3D seismic reflection dataset to determine the external geometries and  
153 geomorphology of the imaged deep-marine deposits (Brown, 2011; Chopra and Marfurt,

154 2007). The dimensions of the MTC-hosted blocks have been quantitatively analysed based on  
155 their morphological characteristics: (i) *block height*, which is the height between the crest and  
156 base of the blocks (i.e. the MTC basal shear surface); (ii) *block spacing*, which is the spacing  
157 between the middle of the crests of two adjacent blocks; (iii) *block tip angle*, which is the  
158 angle between the block tip and vertical; and (iv) *block friction angle*, which is the angle  
159 between the side of the blocks relative to their base surface (see Figure 6b).

## 160 Seismic-stratigraphic analysis

161 We identified and mapped four key horizons (H1-H4) in this study based on their strong  
162 amplitude, continuity (i.e. they are regionally mappable and extend across the study area),  
163 and stratigraphic distribution (i.e. they are relatively evenly distributed throughout the  
164 stratigraphic succession of interest). Horizon H1 (Figure 2b) is a regionally mappable  
165 unconformity that defines the base of the Late Miocene, and which formed as the result of  
166 the collision of the Australian and Eurasian plates (Boyd et al., 1993; Hull and Griffiths, 2002).

## 167 SU-1 and SU-2

168 We divide the studied stratigraphic interval into three seismic units (SU-1-3). SU-1 is c. 500 m  
169 thick near the axis of the Kangaroo syncline, thinning westward and eastward to c. 200 m. SU-  
170 1 contains packages of chaotic, medium- to high-amplitude seismic reflections interpreted as  
171 stacked MTCs (Figure 3b-c) (Hengesh et al., 2012; Nugraha et al., 2018). SU-2 is thinner than  
172 SU-1, but also varies in thickness, being slightly thicker near the centre of the Kangaroo  
173 Syncline (c. 60 m) and thinning gradually westward and eastward to c. 30 m (Figure 3b). SU-2  
174 contains two distinct seismic facies: (i) continuous, low- to medium-amplitude, sub-parallel  
175 seismic reflections in the east; and (ii) discontinuous to chaotic seismic facies in the centre  
176 and west (Figure 3b-c). The continuous seismic facies is interpreted as slope-to-basinfloor,  
177 carbonate ooze deposits, whereas the more discontinuous seismic facies is interpreted as  
178 deformed carbonate ooze drape deposits (Nugraha et al., 2018). Variance attribute-based  
179 analysis of the base of SU-2 (Horizon H2) in the central part of the study area reveals a  
180 concentrated high variance response with circular shape in an NW-SE linear trend (Figure 5a).  
181 These high variance circles form bulges in seismic section that are c. 30-70 m in diameter,  
182 disaggregating the overlying strata (see the seismic section in Figure 5a). Based on their size,  
183 geometry, and distribution, these circular bulges are interpreted as fluid expulsion-related

184 pockmarks (e.g. Plaza-Faverola et al., 2011). Fluid escape features such as these are common  
185 on the Exmouth Plateau (i.e. Velayatham et al., 2019; Velayatham et al., 2018).

## 186 SU-3

187 SU-3 is c. 500 m thick in the axis of the Kangaroo Syncline, gradually thinning westward due  
188 to truncation below MTC 3 (Figure 4a, 4b). We identify three distinct seismic facies in SU-3,  
189 which we describe below (pre-MTC 3, MTC 3, and MTC 2; Figure 3b).

### 190 Pre-MTC 3

191 The pre-existing interval defines the eastern part of SU-3 and is characterised by a thin (70 ms  
192 TWT; 25% of the total thickness of SU-3) package of chaotic to discontinuous, low- to medium-  
193 amplitude seismic reflections at its base, which is overlain by a thick (170 ms TWT; 75% of the  
194 total thickness of SU-3) package of continuous-to-locally slightly wavy, low- to medium-  
195 amplitude seismic reflections (Figure 3c). The chaotic seismic facies is interpreted as an MTC  
196 (MTC 1), whereas the continuous seismic facies likely represents carbonate ooze (Figure 3b,  
197 3c) (Nugraha et al., 2018).

### 198 MTC 3

#### 199 Description

200 MTC 3 defines the central part of SU-3, near the axis of the Kangaroo Syncline, where the  
201 seafloor presently dips very gently (c. 0.4°) (Figure 4b). Approximately 1050 km<sup>2</sup> of MTC 3 is  
202 imaged in the 3D seismic data, although 2D seismic data show the deposit covers c. 3600 km<sup>2</sup>  
203 (Figure 4a, 4b; Figure 5b, 5c, 5d). We describe MTC 3 with respect to the following features:  
204 (i) the geometry of its basal shear surface and seismic facies of its substrate, (ii) the seismic  
205 facies and geometrical characteristics of its contained blocks and troughs, and (iii) its overall  
206 geometry and the geometry of its top surface.

#### 207 (i) The basal shear surface and substrate

208 The basal surface of MTC 3 is characterised by a continuous, high-amplitude, positive seismic  
209 reflection (Figure 6a). In the east, this surface merges with the basal shear surface of MTC 1  
210 (Figure 6a). The basal surface of MTC 3 does not contain any seismic-scale erosional features  
211 such as scours, striations, or grooves (Figure 5c, 5d) (e.g. Bull et al., 2009a; Sobiesiak et al.,  
212 2018). As such, it is not easy to determine the MTC transport direction. However, the surface  
213 defines a sharp boundary between different facies (i.e. weakly deformed below and very



214 chaotic above), and the high-amplitude character supports an interpretation of a basal shear  
215 surface (e.g. Wu et al., 2019). The 60 ms TWT thick (c. 60 m) unit immediately underlying and  
216 representing the substrate of MTC 3 ranges from discontinuous and moderately deformed  
217 near the eastern-margin of MTC 3, to chaotic and highly deformed near the proximal part of  
218 the deposit (Figure 6a, 6b).

#### 219 (ii) Blocks and troughs

220 Map-view images show that MTC 3 contains parallel to sub-parallel, block-shaped packages  
221 (Figure 5c, 5d). In seismic cross sections, these form ridge-shaped blocks flanked by troughs  
222 (Figure 6b). The blocks are 210-300 m high, 170-210 m wide, and 800-1200 m long are  
223 relatively undeformed (Figure 6b). The intervening troughs are 160-260 m high, 190-230 m  
224 wide, 800-1200 m long, and are defined by a very chaotic, variable-amplitude seismic facies.

225 All the blocks contain two distinct seismic facies that are similar to those defining undeformed  
226 slope strata outside of the MTC (Figure 6a, 6b). Seismic reflection within the blocks are sub-  
227 horizontal and are approximately parallel to the basal shear surface and underlying substrate  
228 strata. Three seismic reflections, intra-block reflections a-c, are identified within the blocks,  
229 which can be correlated with confidence from block-to-block over a large area (seismic  
230 reflection a-c; Figure 6b). However, the blocks become more disaggregated, and their external  
231 form become less pronounced, adjacent to the headwall in the E and adjacent to its toe in the  
232 SW. Downslope, intra-block reflections a-c become harder to identify and trace (Figure 6c).  
233 The blocks ultimately become extremely chaotic in the distal part of MTC 3, showing similar  
234 facies to MTC 1 (Figure 6c). Upslope, the relationship between the blocks and the undeformed  
235 strata show a clear increasing deformation systematically eastward (Figure 6a).

236 The average tip angle of the blocks is c. 38°, with little variability about this value (Figure 6d).  
237 The angle of the tip to the basal shear surface ranges from 55-80° (average 71°) (Figure 6d).  
238 The height of the blocks gradually decreases downslope to the SW towards the distal end of  
239 MTC 3, from c. 290 m to c. 190 m (Figure 6e). Block spacing increases towards the SW, from  
240 c. 610 m near the centre to c. 760 m near the distal region of MTC 3 (Figure 6e).

241 The intra-block troughs are characterised by moderately discontinuous to chaotic seismic  
242 facies (Figure 6b). By blending variance and amplitude data we see that the troughs contain  
243 numerous 'v'-shaped, vertical to sub-vertical, pipe-liked structures that extend from the basal

244 shear surface of MTC 3 to its top. We refer to these c. 280 m tall, up to 100 m diameter  
245 features as 'subvertical deformation zones' (SDZs) (Figure 7a). Within troughs, seismic  
246 reflections are mostly sub-horizontal and discontinuous, the edge of the reflections can be as  
247 steep as 50° near the trough margin (Figure 7a). Locally, where the magnitude of intra-trough  
248 deformation is low, we can trace seismic reflections from within the troughs into adjacent  
249 blocks (see the coloured dots in Figure 7a). The width of the VDZs increase upward, from c.  
250 40 m at their narrowest basal point to up a few hundreds of metres at their tops (Figure 7b  
251 and c).

### 252 (iii) Top surface

253 The top of MTC 3 is characterised as a rugose low-amplitude, positive seismic reflection. The  
254 crests of intra-MTC blocks define locally positive relief that are onlapped by overlying  
255 reflections, whereas intervening troughs define concave-up structural lows (Figure 6a, 6b).  
256 The VDZs extends throughout the vertical extent of the trough, and reflections onlap the  
257 blocks (Figure 7a).

### 258 Interpretation

259 The similarity in the seismic facies succession characterising the intra-MTC blocks and the  
260 undeformed strata (i.e. a thin MTC overlain by largely undeformed, slope-to-basinfloor strata)  
261 suggest the former are derived from the latter. This is supported by the blocks in the eastern  
262 part of MTC 3 being the same thickness as the laterally adjacent, largely undeformed interval.  
263 We therefore interpret the boundary between MTC 3 and the undeformed strata is the MTC  
264 headwall. The fact we can correlate the intra-MTC seismic horizons (reflection a-c; Figure 6a,  
265 b) within the blocks and flanking, more highly deformed troughs, suggest that the blocks were  
266 initially transported as a coherent mass. The continuity of the intra-block reflections also  
267 indicate that the blocks were only weakly deformed during the transport.

268 We interpret that the westward decrease in block height and spacing, normal to the broadly  
269 NE-trending headwall, suggest MTC 3 was translated westwards, approximately  
270 perpendicular to the depth contour of the interpreted base of the MTC 3 (Figure 5b, 5d). We  
271 also note that the amount of deformation below MTC 3, inferred from the thickness of the  
272 highly deformed package, increases westwards at the transition from beneath the relatively  
273 thin MTC 1, which forms part of the pre-existing, broadly undeformed slope strata, to below

274 the relatively thick MTC 3. The low degree of internal deformation, limited distance from the  
275 headwall, and lack of kinematic indicators, supports an interpretation that the blocks moved  
276 a limited horizontal distance. Therefore, we suspect that the relatively highly deformed  
277 nature of the substrate near the proximal part of MTC 3 may not have been directly caused  
278 by shearing of the substrate by the overlying mass. We instead interpret that this deformation  
279 occurred due to the presence and catastrophic failure of an overpressured substrate by  
280 liquefaction or strain softening, which both would have caused intense stratal disruption.  
281 Similar liquefaction-driven seismic facies (i.e. medium- to high-amplitude, chaotic seismic  
282 reflections) are described in the literature (e.g. Ogata et al., 2014).

283 The moderately-deformed reflections defining the VDZs indicate modest internal  
284 deformation within these areas. We infer that the VDZs represent vertical fluid migration  
285 conduits, which drove fluid expulsion from the underlying, over-pressured substrate (e.g.  
286 Cartwright and Santamarina, 2015; Løseth et al., 2011; Moss and Cartwright, 2010). The  
287 overlying elliptical depressions, which define structural lows along the top of MTC 3, reflect  
288 overburden collapse due to the expulsion, upward migration, and expulsion of deeper  
289 material. Seismic reflections onlapping blocks protruding from the top surface of MTC 3 may  
290 represent the extruded sediments or subsequently deposited deep-water sediment (e.g. Clari  
291 et al., 2004; Roberts et al., 2010; Watkinson and Hall, 2019).

## 292 MTC 2

293 MTC 2 occurs in the western part of SU-3 (Figure 4b, 5c-d). This deposit is deeply eroded on  
294 its NW margin by a subsequent mass failure event (MTC 4), and is hard to differentiate from  
295 MTC 3 in the NE (Figure 4b, 5d). However, the boundary between MTC 2 and 3 can be inferred  
296 from their slightly differing seismic facies; MTC 3 is defined by an overall higher-amplitude,  
297 blockier seismic facies, whereas MTC 2 is defined by overall lower-amplitude, chaotic seismic  
298 facies (Figure 3a-c). MTC 2 has an NW-trending headwall (Figure 8a) and NE-SW trending  
299 lateral margins (Figure 8b), and comprises low- to very low-amplitude, chaotic reflections. In  
300 the northern part of the Kangaroo syncline, MTC 2 increases in thickness away from its  
301 headwall, from c. 70 ms near its headwall (Figure 8a) to c. 200 ms further NE (Figure 8c). The  
302 orientation of the headwall scarp and lateral margins suggest that MTC 3 was transported  
303 towards the NNE, following the overall dip of the Kangaroo Syncline (Figure 4b).

304 Stratigraphic evolution

305 Based on the observations made above, we propose that the study area has experienced  
306 several episodes of slope failure-driven erosion and deposition (Figure 9). First, multiple,  
307 stacked MTCs were deposited (SU1; Figure 9a) that were subsequently draped by carbonate  
308 ooze (SU-2; Fig. 9b). Gas or fluids, sourced from deeper stratigraphic levels, migrated upward  
309 into SU-2 (Figure 9b). During the initial stage of SU-3 deposition, an MTC was emplaced (MTC  
310 1), which was overlain by a thick, carbonate ooze-bearing sequence (Figure 9c). MTC 2 was  
311 subsequently emplaced in the west of the study area (Figure 9d). The removal of sediment  
312 during the evacuation of MTC 2 likely had a debuttreasing effect, promoting subsequent slope  
313 failure and the triggering of MTC 3 through removal of lateral and down-slope confining  
314 support (Figure 9d). As a result of overpressure released by slope failure, sediments extruded  
315 from below MTC 3 were transported upward through, and deposited on top of, the overlying  
316 mass. MTC 4 was subsequently emplaced in the west of the study area on top of MTC 3,  
317 followed by draping of the entire succession by carbonate ooze (Figure 9e).

## 318 Discussion

319 Was MTC 3 emplaced by a creep or spread?

320 Creep is a gravity-driven process, with the updip margins defined by retrogressively formed  
321 faults and folds (Lee and Chough, 2001; Li et al., 2016). In contrast, spreading occurs above a  
322 pre-cursor failure surface, with the failed mass translating laterally and being broken into  
323 blocks and troughs that are bounded by internally generated faults (Micallef et al., 2007).  
324 Subaqueous creep has been reported from relatively steep slopes ( $>3^\circ$ ) (i.e. Shillington et al.,  
325 2012; Silva and Booth, 1984), whereas subaqueous spread is reported from gentler slopes  
326 occur ( $<1^\circ$ ) (i.e. Micallef et al., 2007). Although we have not undertaken a balanced structural  
327 restoration to investigate the slope dip at the time of MTC 3 emplacement, it is likely that,  
328 given its current position beneath the present basin floor, some c. 300 km from the Late  
329 Miocene shelf margin, it was deposited on a gently dipping slope ( $<1^\circ$ ). The coherent blocks  
330 within MTC 3 occur above a low-angle failure surface, suggesting gravity played only a minor  
331 role in their formation, as well as that of the MTC in which they are contained. The blocks are  
332 also bound by numerous sub-parallel faults that are of very similar dip; such features are  
333 strongly characteristic of the deposits of spreads, rather than creep (Micallef et al., 2007).

334 MTC 3 emplacement model

335 Stage 1: Priming

336 Before the emplacement of MTC 3, the basal shear surface of MTC 1 may have represented a  
337 hydraulic boundary between the overlying c. 300 m thick sediment pile, and the underlying  
338 substrate, defined by sharp decrease in permeability and density (i.e. Madhusudhan et al.,  
339 2017; Wu et al., 2019) (Figure 10a, 10b). Excess pore pressure could have built up at this  
340 boundary, driven by the ascent of fluids from the lower SU-2 and SU-1 (Figure 10a and b). The  
341 properties of the biogenic carbonate ooze sediments (i.e. low permeability, high water  
342 content, fine-grained) defining the substrate of the eventual spread may have a direct  
343 contribution to the build-up of pore pressure (Bryn et al., 2005; Bull et al., 2009b; Kvalstad et  
344 al., 2005; Urlaub et al., 2015). There is also ample evidence that during the early Miocene to  
345 Pliocene, the Exmouth Platform was seismically active, with the Kangaroo Syncline  
346 representing an inversion-related structure linked to the collision of the Indo-Australian and  
347 Eurasian plates (Keep et al., 2007). Related seismicity may have reduced the shear strength  
348 of sediments, and built up the pore fluid pressure within the substrate of MTC 3. The  
349 increased pore pressure was transferred laterally westwards away from, and sealed by, the  
350 overlying basal shear surface of MTC 1 (Figure 10a) (see also examples of pore pressure lateral  
351 propagation from Aylsworth and Lawrence, 2003; Legget and LaSalle, 1978).

352 Stage 2: Distal evacuation

353 We suggest that MTC 3 was triggered due to the removal of material from its distal margin by  
354 the emplacement of MTC 2. The absence of a buttress after northward transport would have  
355 removed the lateral confining pressure within the western part of the pre-spread strata to  
356 drive the spreading (Figure 10c). The sediments immediately around the debutressing  
357 became a flow (i.e. slump), due to the biogenic structure of carbonate ooze that is rapidly  
358 destroyed under loading, transitioning from a coherent to fully disaggregated chaotic mass in  
359 a relatively short distance (i.e. 10-20 km; Principaud et al., 2015; Watson et al., 2019).

360 To the east, the sediment pile was primed to fail for the reasons outlined above (i.e. excess  
361 pore pressure; Figure 10a). The low gradient (c. 0.4°) of the basal shear surface of MTC 3 likely  
362 prevented the failure from accelerating and translating a great distance during emplacement.  
363 As a result, the intra-spread blocks stayed relatively intact compared to failures occurring on

364 more steeply dipping slopes (i.e. Hengesh et al., 2013). Onshore and offshore data indicate  
365 that even small amounts of unloading near the down-dip part of the slope can trigger the  
366 formation of spreads (i.e. Broussard and Sarwar, 2013; Kvalstad et al., 2005; Locat et al., 2011;  
367 Micallef et al., 2007).

368 Stage 3: MTC 3 initiation

369 The mass comprising MTC 3 started sliding westward into the new space created by the  
370 movement northwards of MTC 2 (Figure 10c). Additional shearing and deformation below  
371 MTC 3 ruptured the base-MTC 1 seal layer, promoting liquefaction of the substrate in over-  
372 pressured zone, which drove the upward transport of fluids and the formation of large pipe-  
373 like structures.

374 The tip angle ( $\alpha$ ) and the friction angle of the block ( $\beta$ ) follow a relationship of  $\beta \approx 90^\circ - (\alpha/2)$ ,  
375 which aligns with the failure surface angles observed from triaxial experimental tests on intact  
376 natural clays (Locat et al., 2011; Locat et al., 2015). This relationship suggests that internal  
377 shear fractures were generated during spreading. Two sets of hydraulic internal shear  
378 fractures (primary/secondary internal shear fractures) formed and propagated upward due  
379 to the high fluid over-pressure in the substrate (Figure 10c). The primary internal shear  
380 fractures developed a 'V'-shaped geometry, consistent with the predictions of numerical  
381 models of sediment failure (Andresen, 2001; Buss et al., 2019; Dey et al., 2016; Kvalstad et al.,  
382 2005). In between the primary internal shear fractures, smaller secondary shear fractures  
383 propagated upward from the basal shear surface of MTC 3 (e.g. see also the formation process  
384 of the hydraulic fracturing related pipes from Cartwright and Santamarina, 2015; Løseth et al.,  
385 2011). The lateral movement of the spread will increase the shear stress in the substrate of  
386 MTC 3, driving growth of the primary and secondary fractures. Overlying material was  
387 ultimately broken into fracture-bound blocks flanked by troughs.

388 Stage 4: Internal deformation and lateral spreading

389 Overpressured substrate fluid-sediment mixes flowed upward via the secondary internal  
390 shear fractures within sub-circular fluid pipes (e.g. Cartwright and Santamarina, 2015). This  
391 extruded material was deposited in depressions above the troughs on the top surface of MTC  
392 3 (Figure 10d). Blocks near the distal end of MTC 3 underwent a greater lateral displacement  
393 and deformation with increase release of the excess pore pressure from the base of the

394 spread compared to proximal areas that moved less far. Due to the release of overpressure,  
395 the shear stress required to drive horizontal motion increased, which may ultimately stop  
396 spreading. The spreading may also stop because the mass hit the far (eastern) of the existing  
397 MTC 2 lateral margin (Figure 10d). There is an increasing deformation near the headwall of  
398 the spread. This is due to the failed sediments of MTC 3 moved west first, this might have  
399 ended up with a 'hole' in the east near the initial scarp. The initial scarp was later failed  
400 retrogressively, leaving a step-like headwall scarp, and a mass of strongly deformed  
401 sediments next to the headwall (Figure 10d).

402 Implications

403 *Preconditioning and triggering of spreads: Unloading and lubrication*

404 We have investigated the geometry and internal structure of an MTC, inferring it was related  
405 to a submarine spread. Our study shows that, in these cases, spreading can occur even if the  
406 slope gradient is presently low. We propose that the spread was *primed* by the presence of  
407 an overpressured layer, which acts as a basal shear surface and promotes sliding on a very  
408 low-angle slope. Slope failure was ultimately *triggered* by debuttreasing of the slope mass by  
409 an earlier slide, which removed downslope and/or lateral confinement. Together these  
410 processes resulted in a short run-out but highly deformed slide mass. While the spread shows  
411 abundant evidence for intense internal deformation, we relate this deformation to fluid  
412 escape from subsurface overpressured strata beneath the failing mass, rather than to  
413 landslide disaggregation under rapid, long-distance transport. We suggest that the slide mass  
414 may have only moved a relatively short distance (i.e. only a few hundred metres) and that the  
415 amount of strain observed in landslides is therefore not necessarily a direct indication of  
416 transport distance.

417 *The importance of rheology and mobility for geohazard assessments*

418 For offshore geohazard assessments it is important to understand the mobility and rheology  
419 of an MTC (Thomas et al., 2010). If the landslide mass of MTC 3 moved only a short distance  
420 and at relatively low speed, then the potential for tsunamigenesis will be low, despite the  
421 relatively large volume (c. 360 km<sup>3</sup>) of the mass. Numerical modelling has shown that very  
422 large landslides (volumes of up to 1000 km<sup>3</sup>) may not trigger a tsunami if they commence as  
423 relatively slow, retrogressive failures (Løvholt et al., 2017).

424 The nature of seafloor and subsurface deformation associated with submarine landsliding  
425 control the impact this processes has on different offshore structures. For instance, a seabed-  
426 laid pipeline or cable may be able to withstand slow-moving seafloor displacement during a  
427 spread, instead being much more vulnerable to the impact of faster-moving slides that  
428 become frontally emergent and disaggregate to form more mobile debris flows (Lacroix et al.,  
429 2020; Thomas et al., 2010; Zakeri, 2009). Piles or top-hole conductors that support platforms  
430 or deep-sea field developments may penetrate tens or hundreds of metres below the seafloor.  
431 These deeper foundations are susceptible to i) lateral and vertical movements, which may be  
432 relatively limited within intact blocks due to the limited transport distance of the MTC; and ii)  
433 changes in subsurface pore pressure and the remoulding of sediments, which together may  
434 reduce their lateral capacity (i.e. weakening their support); this particularly property may be  
435 prognosed by when an intra-block, fluid vertical fluid venting system is identified  
436 (Amaratunga and Grozic, 2009; Hong et al., 2017).

#### 437 *Submarine spreads: Underappreciated agents for seafloor fluid flow*

438 Many studies propose fluid migration at depth as a potential preconditioning or triggering  
439 factor for MTCs (e.g. Bünz et al., 2005; Deville et al., 2020; Elger et al., 2018); however, few  
440 studies link MTCs to syn- or post-emplacment release of fluids (e.g. Bøe et al., 2012; Browne  
441 et al., 2020). It is suggested that significant volumes of methane (an important greenhouse  
442 gas) may have been emitted during the disaggregation of the 3000 km<sup>3</sup> Storegga Slide (Paull  
443 et al., 2007), and that methane release by widespread submarine landslide activity may have  
444 been a contributory mechanism for elevated methane emissions that catalysed the  
445 Palaeocene-Eocene Thermal maximum (Higgins and Schrag, 2006). The role of submarine  
446 landslides in the release of previously sequestered fluids such as methane remains poorly  
447 constrained, and is thus omitted from existing global budgets. Our study shows that fluid  
448 escape can play an important role during MTC emplacement, as vertical escape structures act  
449 as efficient conduits for fluids and sediments from depth to the seafloor. Similar seafloor fluid  
450 expulsions, including that linked to post-MTC emplacement, create cold seeps that support  
451 high biomass communities of microbes and chemosynthetic fauna, as the focused fluid flow  
452 creates cold seeps (e.g. Deville et al., 2020). Therefore, as well as disturbing the seafloor,  
453 MTCs may also provide important hotspots for deep-sea biodiversity, particularly where they  
454 create focused zones of fluid flow.



## 455 Conclusion

456 We use 2D and 3D seismic reflection data to investigate processes of submarine spreading,  
457 on the Exmouth Plateau, offshore NW Australia. The spread comprises: (i) giant, upward-  
458 tapering blocks (c. 300 m-high, c. 1200 m-long, and c. 210 m-wide) which are undeformed,  
459 and (ii) intervening troughs (c. 260 m depressions separating the blocks), which are  
460 moderately deformed. We interpret that the blocks were only transported minimal lateral  
461 distance, and the relatively deformed troughs are formed by the expulsion of fluid and  
462 sediment during hydraulic failure of the sediment mass. We then developed a new internal  
463 hydraulic fracturing model that accounts for the styles and patterns of blocks and the  
464 intervening troughs. The new model requires a low gradient prerequisite over-pressured  
465 failure surface/zone, the low gradient of the basal shear surface likely prevented the block  
466 from accelerating and translating a great distance during emplacement. The new model  
467 suggests that the spread is initiated by the removal of materials in the toe of the otherwise  
468 stable strata (i.e. debuttrressing). The debuttrressing of the adjacent strata results in the  
469 decrease of the lateral confining pressure within the pre-spread strata, and subsequently,  
470 triggers the spreading process. The underlying overpressured layer is important to prime the  
471 spreading and explain the scale and style of fluid escape. An improved understanding of the  
472 initiation, emplacement and deposition of submarine spreading failures adds to our broader  
473 understanding of deep-water mass failure processes, the risks posed to seafloor  
474 infrastructure, and the often-complex interactions with local benthic ecology.

## 475 Acknowledgements

476 The authors would like to thank Geoscience Australia for providing the 2D and 3D seismic  
477 reflection data that was used in this study, and Schlumberger are thanked for providing Petrel  
478 to Imperial College. The first author thanks the Chinese Scholar Council and iRock Technology  
479 for its financial support. The fifth author acknowledges funding from the Natural Environment  
480 Research Council CLASS National Capability Programme (NE/R015953/1). The seventh author  
481 thanks for funding from Guangdong Basic and Applied Basic Research Foundation  
482 (2020B1515020016).

483 Reference

484 Alves, T. M., 2015, Submarine slide blocks and associated soft-sediment deformation in deep-water  
485 basins: a review: *Marine and Petroleum Geology*, v. 67, p. 262-285.

486 Amaratunga, A., and J. Grozic, 2009, On the undrained unloading behaviour of gassy sands: *Canadian*  
487 *Geotechnical Journal*, v. 46, p. 1267-1276.

488 Andresen, L., 2001, Effect of strain softening on stability analyses: Analysis of retrogressive sliding  
489 due to strain softening—Ormen Lange case study. NGI report.

490 Aylsworth, J., and D. Lawrence, 2003, Earthquake-induced landsliding east of Ottawa; a contribution  
491 to the Ottawa Valley Landslide Project: *Geohazards 2003*, 3rd Canadian Conference on  
492 Geotechnique and Natural Hazards/3ième Conférence canadienne sur la géotechnique et les  
493 risques naturels; Edmonton, Alberta; CA; June 9-10 juin 2003.

494 Bøe, R., V. K. Bellec, L. Rise, L. Buhl-Mortensen, S. Chand, and T. Thorsnes, 2012, Catastrophic fluid  
495 escape venting-tunnels and related features associated with large submarine slides on the  
496 continental rise off Vesterålen–Troms, North Norway: *Marine and petroleum geology*, v. 38,  
497 p. 95-103.

498 Boyd, R., P. Williamson, and B. Haq, 1993, Seismic Stratigraphy and Passive - Margin Evolution of the  
499 Southern Exmouth Plateau: *Sequence Stratigraphy and Facies Associations*, p. 579-603.

500 Bradley, K., R. Mallick, H. Andikagumi, J. Hubbard, E. Meilianda, A. Switzer, N. Du, G. Brocard, D.  
501 Alfian, and B. Benazir, 2019, Earthquake-triggered 2018 Palu Valley landslides enabled by  
502 wet rice cultivation: *Nature Geoscience*, v. 12, p. 935-939.

503 Broussard, R., and A. K. Sarwar, 2013, A Structural Analysis of the Green Knoll Salt Dome Located in  
504 Southeast Green Canyon, Gulf of Mexico.

505 Brown, A. R., 2011, Interpretation of three-dimensional seismic data, *Society of Exploration*  
506 *Geophysicists and American Association of Petroleum Geologists*.

507 Browne, G., S. Bull, M. Arnot, A. Boyes, P. King, and K. Helle, 2020, The role of mass transport  
508 deposits contributing to fluid escape: Neogene outcrop and seismic examples from north  
509 Taranaki, New Zealand: *GML*.

510 Bryn, P., K. Berg, C. F. Forsberg, A. Solheim, and T. J. Kvalstad, 2005, Explaining the Storegga slide:  
511 *Marine and Petroleum Geology*, v. 22, p. 11-19.

512 Bull, S., J. Cartwright, and M. Huuse, 2009a, A review of kinematic indicators from mass-transport  
513 complexes using 3D seismic data: *Marine and Petroleum Geology*, v. 26, p. 1132-1151.

514 Bull, S., J. Cartwright, and M. Huuse, 2009b, A subsurface evacuation model for submarine slope  
515 failure: *Basin Research*, v. 21, p. 433-443.

516 Bünz, S., J. Mienert, P. Bryn, and K. Berg, 2005, Fluid flow impact on slope failure from 3D seismic  
517 data: a case study in the Storegga Slide: *Basin Research*, v. 17, p. 109-122.

518 Buss, C., B. Friedli, and A. M. Puzrin, 2019, Kinematic energy balance approach to submarine  
519 landslide evolution: *Canadian Geotechnical Journal*, v. 56, p. 1351-1365.

520 Cartwright, J., and C. Santamarina, 2015, Seismic characteristics of fluid escape pipes in sedimentary  
521 basins: implications for pipe genesis: *Marine and Petroleum Geology*, v. 65, p. 126-140.

522 Chaytor, J. D., W. E. Baldwin, S. J. Bentley, M. Damour, D. Jones, J. Maloney, M. D. Miner, J. Obelcz,  
523 and K. Xu, 2020, Short-and long-term movement of mudflows of the Mississippi River Delta  
524 Front and their known and potential impacts on oil and gas infrastructure: *Geological*  
525 *Society, London, Special Publications*, v. 500, p. 587-604.

526 Chopra, S., and K. J. Marfurt, 2007, Seismic attributes for prospect identification and reservoir  
527 characterization, *Society of Exploration Geophysicists and European Association of*  
528 *Geoscientists and Engineers*.

529 Clari, P., S. Cavagna, L. Martire, and J. Hunziker, 2004, A Miocene mud volcano and its plumbing  
530 system: a chaotic complex revisited (Monferrato, NW Italy): *Journal of Sedimentary*  
531 *Research*, v. 74, p. 662-676.

532 Cruden, D. M., and D. J. Varnes, 1996, Landslides: investigation and mitigation. Chapter 3-Landslide  
533 types and processes: Transportation research board special report.

534 De Blasio, F. V., and A. Elverhoi, 2011, Properties of mass-transport deposits as inferred from  
535 dynamic modeling of subaqueous mass wasting: a short review: Mass Transport Deposits in  
536 Deepwater Settings: SEPM Special Publication, v. 96, p. 499-508.

537 Deville, E., C. Scalabrin, G. Jouet, A. Cattaneo, A. Battani, S. Noirez, H. Vermesse, K. Olu, L. Corbari,  
538 and M. Boulard, 2020, Fluid seepage associated with slope destabilization along the Zambezi  
539 margin (Mozambique): Marine Geology, p. 106275.

540 Dey, R., B. Hawlader, R. Phillips, and K. Soga, 2016, Numerical modelling of submarine landslides  
541 with sensitive clay layers: Géotechnique, v. 66, p. 454-468.

542 Dutta, S., and B. Hawlader, 2019, Pipeline–soil–water interaction modelling for submarine landslide  
543 impact on suspended offshore pipelines: Géotechnique, v. 69, p. 29-41.

544 Elger, J., C. Berndt, L. Rüpke, S. Krastel, F. Gross, and W. H. Geissler, 2018, Submarine slope failures  
545 due to pipe structure formation: Nature communications, v. 9, p. 1-6.

546 Exxon, N., B. Haq, and U. Von Rad, 1992, Exmouth Plateau revisited: scientific drilling and geological  
547 framework: Proceedings of the Ocean Drilling Program, Scientific Results, p. 3-20.

548 Falvey, D., and J. Veevers, 1974, Physiography of the Exmouth and Scott plateaus, western Australia,  
549 and adjacent northeast Wharton Basin: Marine Geology, v. 17, p. 21-59.

550 Geertsema, M., A. Blais-Stevens, E. Kwooll, B. Menounos, J. G. Venditti, A. Grenier, and K. Wiebe,  
551 2018, Sensitive clay landslide detection and characterization in and around Lakelse Lake,  
552 British Columbia, Canada: Sedimentary geology, v. 364, p. 217-227.

553 Haq, B. U., R. L. Boyd, N. F. Exxon, and U. von Rad, 1992, 47. EVOLUTION OF THE CENTRAL EXMOUTH  
554 PLATEAU: A POST-DRILLING PERSPECTIVE1.

555 Hengesh, J., J. Dirstein, and A. Stanley, 2013, Landslide geomorphology along the Exmouth plateau  
556 continental margin, North West Shelf, Australia: Australian Geomechanics Journal, v. 48, p.  
557 71-92.

558 Hengesh, J., J. K. Dirstein, and A. J. Stanley, 2012, Seafloor geomorphology and submarine landslide  
559 hazards along the continental slope in the Carnarvon Basin, Exmouth Plateau, North West  
560 Shelf, Australia: The APPEA Journal, v. 52, p. 493-512.

561 Hong, Y., L. Wang, C. W. Ng, and B. Yang, 2017, Effect of initial pore pressure on undrained shear  
562 behaviour of fine-grained gassy soil: Canadian Geotechnical Journal, v. 54, p. 1592-1600.

563 Hull, J., and C. Griffiths, 2002, Sequence stratigraphic evolution of the Albian to Recent section of the  
564 Dampier Sub-basin, North West Shelf, Australia, PhD thesis 1999. University of Adelaide,  
565 Australia.

566 Jackson, C. A., 2011, Three-dimensional seismic analysis of megaclast deformation within a mass  
567 transport deposit; implications for debris flow kinematics: Geology, v. 39, p. 203-206.

568 Keep, M., M. Harrowfield, and W. Crowe, 2007, The neogene tectonic history of the North West  
569 Shelf, Australia: Exploration Geophysics, v. 38, p. 151-174.

570 Kvalstad, T. J., L. Andresen, C. F. Forsberg, K. Berg, P. Bryn, and M. Wangen, 2005, The Storegga slide:  
571 evaluation of triggering sources and slide mechanics: Marine and Petroleum Geology, v. 22,  
572 p. 245-256.

573 Lacroix, P., A. L. Handwerger, and G. Bièvre, 2020, Life and death of slow-moving landslides: Nature  
574 Reviews Earth & Environment.

575 Lee, S., and S. Chough, 2001, High - resolution (2 - 7 kHz) acoustic and geometric characters of  
576 submarine creep deposits in the South Korea Plateau, East Sea: Sedimentology, v. 48, p. 629-  
577 644.

578 Legget, R. F., and P. LaSalle, 1978, Soil studies at Shipshaw, Quebec: 1941 and 1969: Canadian  
579 Geotechnical Journal, v. 15, p. 556-564.

580 Li, W., T. M. Alves, S. Wu, M. Rebesco, F. Zhao, L. Mi, and B. Ma, 2016, A giant, submarine creep zone  
581 as a precursor of large-scale slope instability offshore the Dongsha Islands (South China Sea):  
582 Earth and Planetary Science Letters, v. 451, p. 272-284.

583 Locat, A., S. Leroueil, S. Bernander, D. Demers, H. P. Jostad, and L. Ouehb, 2011, Progressive failures  
584 in eastern Canadian and Scandinavian sensitive clays: *Canadian Geotechnical Journal*, v. 48,  
585 p. 1696-1712.

586 Locat, A., S. Leroueil, A. Fortin, D. Demers, and H. P. Jostad, 2015, The 1994 landslide at Sainte-  
587 Monique, Quebec: geotechnical investigation and application of progressive failure analysis:  
588 *Canadian Geotechnical Journal*, v. 52, p. 490-504.

589 Løseth, H., L. Wensaas, B. Arntsen, N.-M. Hanken, C. Basire, and K. Graue, 2011, 1000 m long gas  
590 blow-out pipes: *Marine and Petroleum Geology*, v. 28, p. 1047-1060.

591 Løvholt, F., S. Bondevik, J. S. Laberg, J. Kim, and N. Boylan, 2017, Some giant submarine landslides do  
592 not produce large tsunamis: *Geophysical Research Letters*, v. 44, p. 8463-8472.

593 Madhusudhan, B., M. Clare, C. Clayton, and J. Hunt, 2017, Geotechnical profiling of deep-ocean  
594 sediments at the AFEN submarine slide complex: *Quarterly Journal of Engineering Geology  
595 and Hydrogeology*, v. 50, p. 148-157.

596 Maher, B. A., and R. Thompson, 1999, *Quaternary climates, environments and magnetism*,  
597 Cambridge University Press.

598 Masson, D., C. Harbitz, R. Wynn, G. Pedersen, and F. Løvholt, 2006, Submarine landslides: processes,  
599 triggers and hazard prediction: *Philosophical Transactions of the Royal Society A:  
600 Mathematical, Physical and Engineering Sciences*, v. 364, p. 2009-2039.

601 Micallef, A., D. G. Masson, C. Berndt, and D. A. Stow, 2007, Morphology and mechanics of submarine  
602 spreading: A case study from the Storegga Slide: *Journal of Geophysical Research: Earth  
603 Surface*, v. 112.

604 Moss, J., and J. Cartwright, 2010, 3D seismic expression of km - scale fluid escape pipes from  
605 offshore Namibia: *Basin Research*, v. 22, p. 481-501.

606 Nemeč, W., 1990, Aspects of sediment movement on steep delta slopes: *Coarse-grained deltas*, v.  
607 10, p. 29-73.

608 Nugraha, H. D., C. A.-L. Jackson, H. D. Johnson, D. M. Hodgson, and M. Clare, 2019, How erosive are  
609 submarine landslides?

610 Nugraha, H. D., C. A. L. Jackson, H. D. Johnson, D. M. Hodgson, and M. T. Reeve, 2018, Tectonic and  
611 oceanographic process interactions archived in Late Cretaceous to Present deep - marine  
612 stratigraphy on the Exmouth Plateau, offshore NW Australia: *Basin Research*.

613 Ogata, K., J. Mountjoy, G. A. Pini, A. Festa, and R. Tinterri, 2014, Shear zone liquefaction in mass  
614 transport deposit emplacement: A multi-scale integration of seismic reflection and outcrop  
615 data: *Marine Geology*, v. 356, p. 50-64.

616 Paull, C., W. Ussler, and W. Holbrook, 2007, Assessing methane release from the colossal Storegga  
617 submarine landslide: *Geophysical research letters*, v. 34.

618 Plaza-Faverola, A., S. Bünz, and J. Mienert, 2011, Repeated fluid expulsion through sub-seabed  
619 chimneys offshore Norway in response to glacial cycles: *Earth and Planetary Science Letters*,  
620 v. 305, p. 297-308.

621 Pope, E. L., P. J. Talling, and L. Carter, 2017, Which earthquakes trigger damaging submarine mass  
622 movements: Insights from a global record of submarine cable breaks?: *Marine Geology*, v.  
623 384, p. 131-146.

624 Posamentier, H. W., and O. J. Martinsen, 2011, The character and genesis of submarine mass-  
625 transport deposits: insights from outcrop and 3D seismic data: *Mass-transport deposits in  
626 deepwater settings: Society for Sedimentary Geology (SEPM) Special Publication 96*, p. 7-38.

627 Principaud, M., T. Mulder, H. Gillet, and J. Borgomano, 2015, Large-scale carbonate submarine mass-  
628 wasting along the northwestern slope of the Great Bahama Bank (Bahamas): Morphology,  
629 architecture, and mechanisms: *Sedimentary Geology*, v. 317, p. 27-42.

630 Randolph, M. F., and D. J. White, 2012, Interaction forces between pipelines and submarine slides—  
631 A geotechnical viewpoint: *Ocean Engineering*, v. 48, p. 32-37.

632 Roberts, K., R. Davies, and S. Stewart, 2010, Structure of exhumed mud volcano feeder complexes,  
633 Azerbaijan: *Basin Research*, v. 22, p. 439-451.

634 Savage, W. Z., and D. J. Varnes, 1987, Mechanics of gravitational spreading of steep-sided ridges  
635 («sackung»): Bulletin of the International Association of Engineering Geology-Bulletin de  
636 l'Association Internationale de Géologie de l'Ingénieur, v. 35, p. 31-36.

637 Scarselli, N., K. McClay, and C. Elders, 2013, Submarine slide and slump complexes, Exmouth Plateau,  
638 NW Shelf of Australia: The Sedimentary Basins of Western Australia IV: Proceedings of the  
639 Petroleum Exploration Society of Australia Symposium, Perth, WA.

640 Shillington, D. J., L. Seeber, C. C. Sorlien, M. S. Steckler, H. Kurt, D. Dondurur, G. Cifci, C. Imren, M.-H.  
641 Cormier, and C. McHugh, 2012, Evidence for widespread creep on the flanks of the Sea of  
642 Marmara transform basin from marine geophysical data: *Geology*, v. 40, p. 439-442.

643 Silva, A. J., and J. S. Booth, 1984, Creep behavior of submarine sediments: *Geo-marine letters*, v. 4, p.  
644 215-219.

645 Sobiesiak, M. S., B. Kneller, G. I. Alsop, and J. P. Milana, 2018, Styles of basal interaction beneath  
646 mass transport deposits: *Marine and Petroleum Geology*, v. 98, p. 629-639.

647 Strasser, M., M. Kölling, C. d. S. Ferreira, H. G. Fink, T. Fujiwara, S. Henkel, K. Ikehara, T. Kanamatsu,  
648 K. Kawamura, and S. Kodaira, 2013, A slump in the trench: Tracking the impact of the 2011  
649 Tohoku-Oki earthquake: *Geology*, v. 41, p. 935-938.

650 Tappin, D., 2010, Submarine mass failures as tsunami sources: their climate control: *Philosophical  
651 Transactions of the Royal Society A: Mathematical, Physical and Engineering Sciences*, v. 368,  
652 p. 2417-2434.

653 Thomas, S., J. Hooper, and M. Clare, 2010, Constraining geohazards to the past: impact assessment  
654 of submarine mass movements on seabed developments, *Submarine mass movements and  
655 their consequences*, Springer, p. 387-398.

656 Urlaub, M., P. J. Talling, and D. G. Masson, 2013, Timing and frequency of large submarine  
657 landslides: implications for understanding triggers and future geohazard: *Quaternary Science  
658 Reviews*, v. 72, p. 63-82.

659 Urlaub, M., P. J. Talling, A. Zervos, and D. Masson, 2015, What causes large submarine landslides on  
660 low gradient ( $< 2^\circ$ ) continental slopes with slow ( $\sim 0.15$  m/kyr) sediment accumulation?:  
661 *Journal of Geophysical Research: Solid Earth*, v. 120, p. 6722-6739.

662 Varnes, D. J., 1978, Slope movement types and processes: Special report, v. 176, p. 11-33.

663 Velayatham, T., S. Holford, M. Bunch, R. King, and C. Magee, 2019, 3D Seismic Analysis of Ancient  
664 Subsurface Fluid Flow in the Exmouth Plateau, Offshore Western Australia.

665 Velayatham, T., S. P. Holford, and M. A. Bunch, 2018, Ancient fluid flow recorded by remarkably  
666 long, buried pockmark trains observed in 3D seismic data, Exmouth Plateau, Northern  
667 Carnarvon basin: *Marine and Petroleum Geology*, v. 95, p. 303-313.

668 von Rad, U., Haq, B.U., et al., 1992, Proceedings of the Ocean Program, Scientific Results: Ocean  
669 Drilling Program, v. Leg 122.

670 Watkinson, I. M., and R. Hall, 2019, Impact of communal irrigation on the 2018 Palu earthquake-  
671 triggered landslides: *Nature Geoscience*, v. 12, p. 940-945.

672 Watson, P., F. Bransby, Z. L. Delimi, C. Erbrich, M. Randolph, M. Rattley, M. Silva, B. Stevens, S.  
673 Thomas, and Z. Westgate, 2019, Foundation design in offshore carbonate sediments–  
674 building on knowledge to address future challenges: From Research to Applied Geotechnics:  
675 Invited Lectures of the XVI Pan-American Conference on Soil Mechanics and Geotechnical  
676 Engineering (XVI PCSMGE), 17-20 November 2019, Cancun, Mexico, p. 240.

677 Watts, P., S. T. Grilli, D. R. Tappin, and G. J. Fryer, 2005, Tsunami generation by submarine mass  
678 failure. II: Predictive equations and case studies: *Journal of waterway, port, coastal, and  
679 ocean engineering*, v. 131, p. 298-310.

680 Wu, N., C. A. Jackson, H. Johnson, and D. M. Hodgson, 2019, Lithological, petrophysical and seal  
681 properties of mass-transport complexes (MTCs), northern Gulf of Mexico: *EarthArXiv*.  
682 February, v. 19.

683 Zakeri, A., 2009, Review of state-of-the-art: Drag forces on submarine pipelines and piles caused by  
684 landslide or debris flow impact: *Journal of offshore mechanics and Arctic engineering*, v. 131.

685 Zhu, H., and M. F. Randolph, 2010, Large deformation finite-element analysis of submarine landslide  
686 interaction with embedded pipelines: *International Journal of Geomechanics*, v. 10, p. 145-  
687 152.

688 Figure caption

689 Figure 1 Schematic diagram showing the classification of mass-transport complexes adopted  
690 in this study (modified from Nemec, 1990; Posamentier and Martinsen, 2011; Scarselli et al.,  
691 2013).

692 Figure 2 a) Regional map of the study area showing the location of the Exmouth Plateau Arch,  
693 Kangaroo Syncline. The white and grey lines represent 2D seismic reflection data, and the red  
694 polygon represents the location of 3D seismic reflection dataset. Shaded relief GEBCO\_2014  
695 bathymetry map downloaded from <https://www.ngdc.noaa.gov/maps/autogrid/>; b) location  
696 map of the figures demonstrated in this study; c) Stratigraphy column and the major tectonic  
697 event of the study interval; d) Sketch map of the regional structures crossing the study area,  
698 showing the modern depositional systems, adapted from Nugraha et al. (2018).

699 Figure 3 a) Un-interpreted regional seismic section; b) Interpreted regional seismic section  
700 highlighting the key horizons and the seismic units the study area, note that the horizon H1 is  
701 the same horizon of Horizon C (see detail from Nugraha et al., 2018) which defines an  
702 unconformity of late Miocene (~9 Ma); c) Interpretation sketch of the regional seismic section.  
703 See Figure 2b for location.

704 Figure 4 a) Regional structure map interpreted based on the 2D and 3D seismic reflection data,  
705 showing the depth structure calculated on horizon H3; b) sketch of the regional structure map  
706 showing the distribution of the key intervals in SU-3 (undeformed strata, MTC 3, and MTC 2).

707 Figure 5 a) Variance attribute calculated on Horizon H2 within the 3D seismic reflection data  
708 area, revealing pipe-like structures. The dashed line indicates the same boundary in Figure 5d  
709 between the undeformed and deformed strata. The upper left map shows the zoom-in view  
710 of pipe-like structures, and the upper right seismic section shows the seismic cross-section of  
711 the fluid pipe; b) depth structure map calculated on basal shear surface of the MTC 3 within  
712 the 3D seismic area; c) variance attribute calculated on Horizon H3 within 3D seismic area; d)  
713 sketch of the MTC 3 deposit, revealing the key intervals in SU-3 (undeformed strata, spread,  
714 and MTCs).

715 Figure 6 a) Seismic section showing the eastern boundary of the MTC 3 and the undeformed  
716 strata; b) seismic section showing the proximal section of the MTC 3; c) seismic section  
717 showing the distal section of the MTC 3. See the location from Figure 5d; d) the calculation of  
718 the tip angle ( $\alpha$ ) of the blocks, and the friction angle of the blocks to the failure surface ( $\beta$ ); e)  
719 the calculation of height and the spacing of the blocks. See block number from Figure 6b and  
720 6c, and the blocks number refers to the order in which the blocks are away from the  
721 undeformed strata.

722 Figure 7 a) Seismic characteristics of pipe structures in the seismic section with an overlay of  
723 the variance attribute, and a zoomed-in view of the VDZs, showing the details of the pipe like  
724 fluid escape structures, see the location in Figure 6b; b) variance time slice through the  
725 troughs, showing the crater shaped pipes; c) structure map of the horizon H3, showing the  
726 top structure of the MTC 3, see the location in Figure 7a. The diameters of the crater-shaped  
727 depressions increase upward, from c. 80 m in the variance time slice to hundreds of metres  
728 in the structure map.

729 Figure 8 a) Seismic cross-section through the headwall scarp area of MTC 2; b) seismic cross-  
730 section through the lateral margins of MTC 2; c) seismic cross-section through the body of  
731 MTC 2.

732 Figure 9 Stratigraphic evolution of the study area. a) Seismic unit 1 (SU-1), mainly comprises  
733 chaotic seismic reflections and deposited as MTCs; b) seismic unit 2 (SU-2), mainly consist of  
734 well-layered seismic section and deposited as carbonate drapes; c) the initial stage of seismic  
735 unit 3 (SU-3), consist MTC 1 and carbonate drapes; d) the following stage of SU-3, consisting  
736 coherent blocks and chaotic intervening troughs; e) the final stage of SU-3, mainly consist  
737 erupted sediments which followed by carbonate drapes.

738 Figure 10 Schematic diagram showing the development of the spread: a) Deposition of the  
739 undeformed sediments, MTC 1 and down dip evacuation of the MTC 3; b) inferred  
740 permeability and shear strength curve through undeformed strata; c) overpressure induced  
741 primary and secondary internal fractures propagation stage; d) sediments dislocated into  
742 blocks and troughs with extruded sediments deposition stage.

743





Figure 1

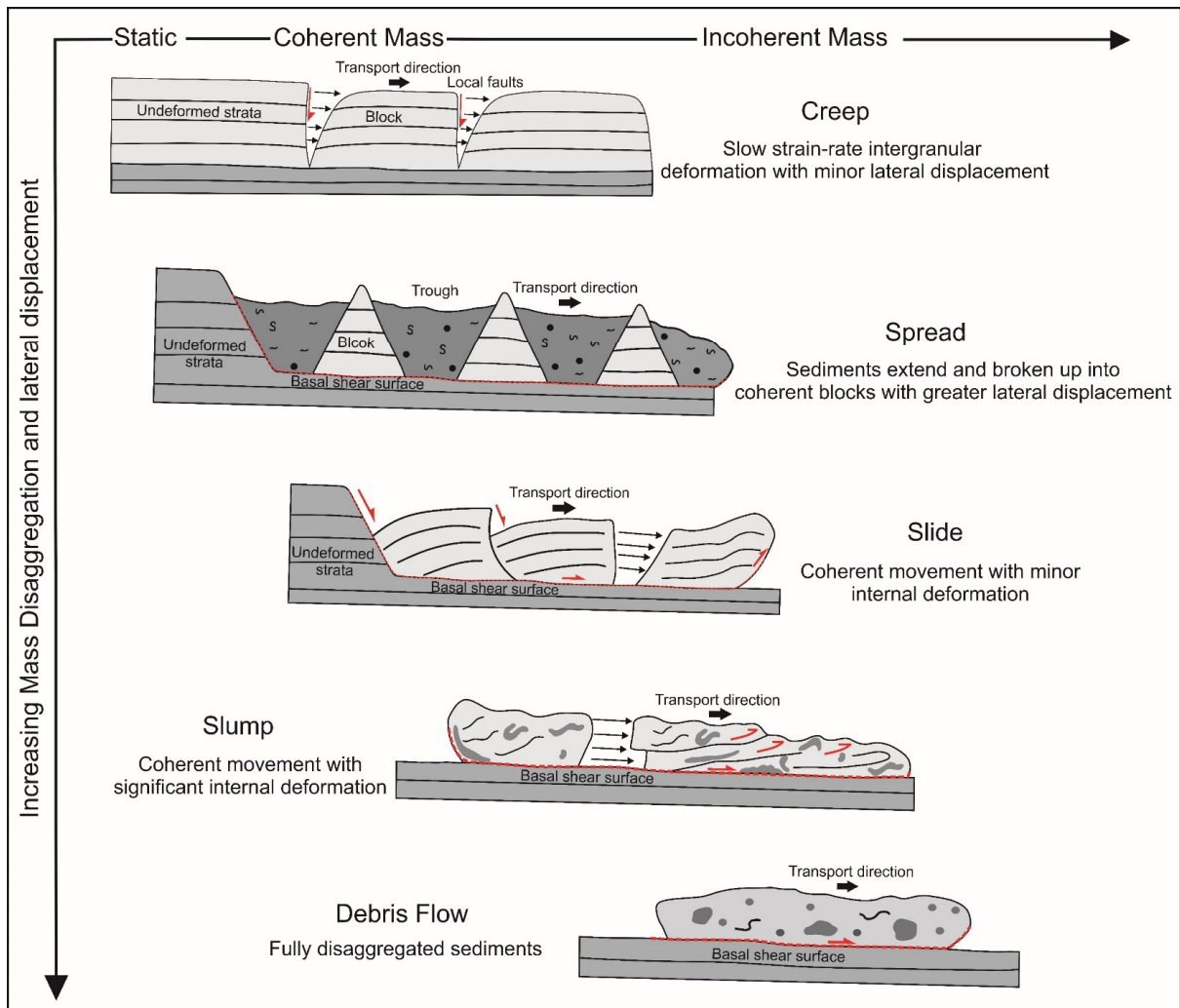


Figure 2

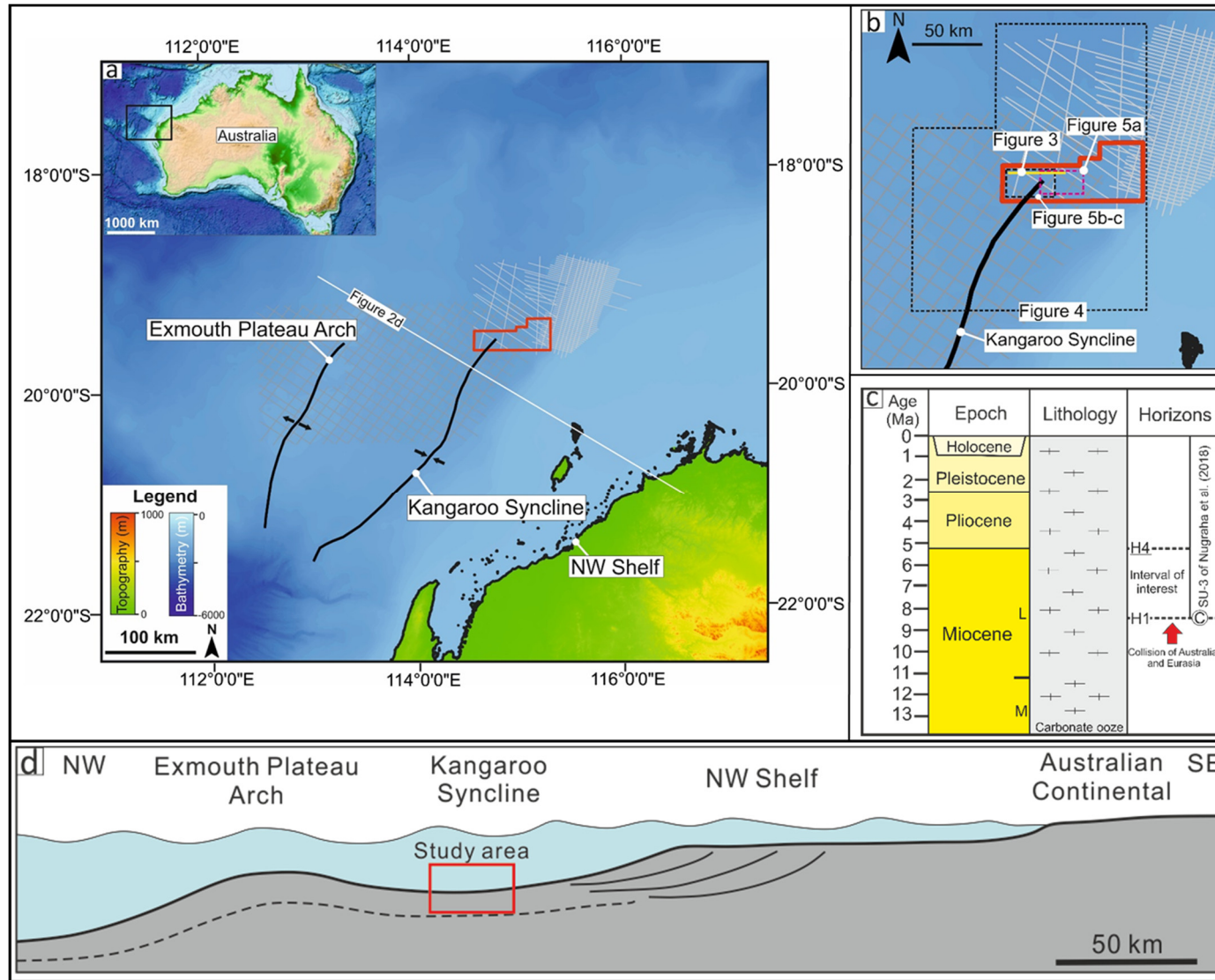


Figure 3

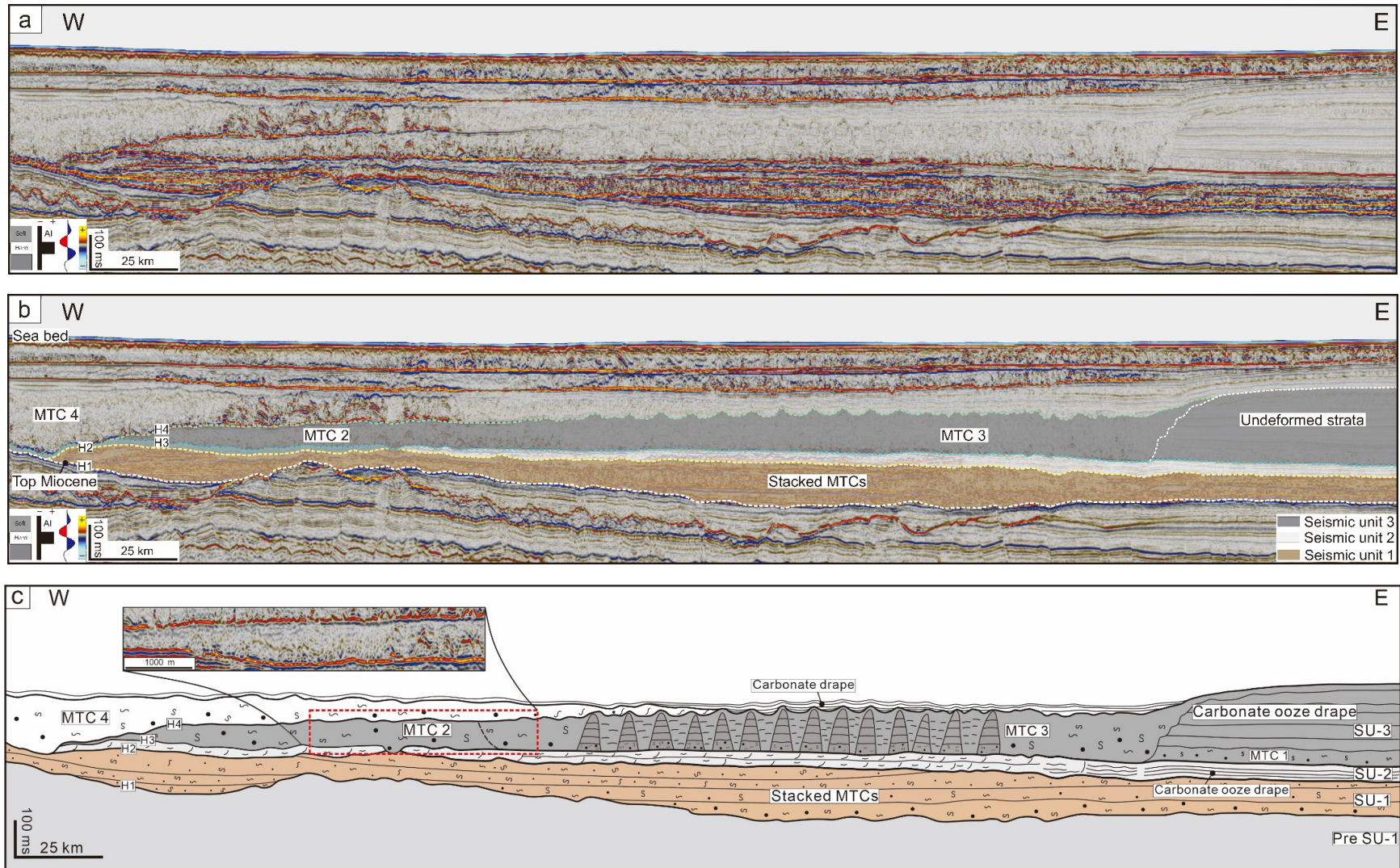




Figure 4

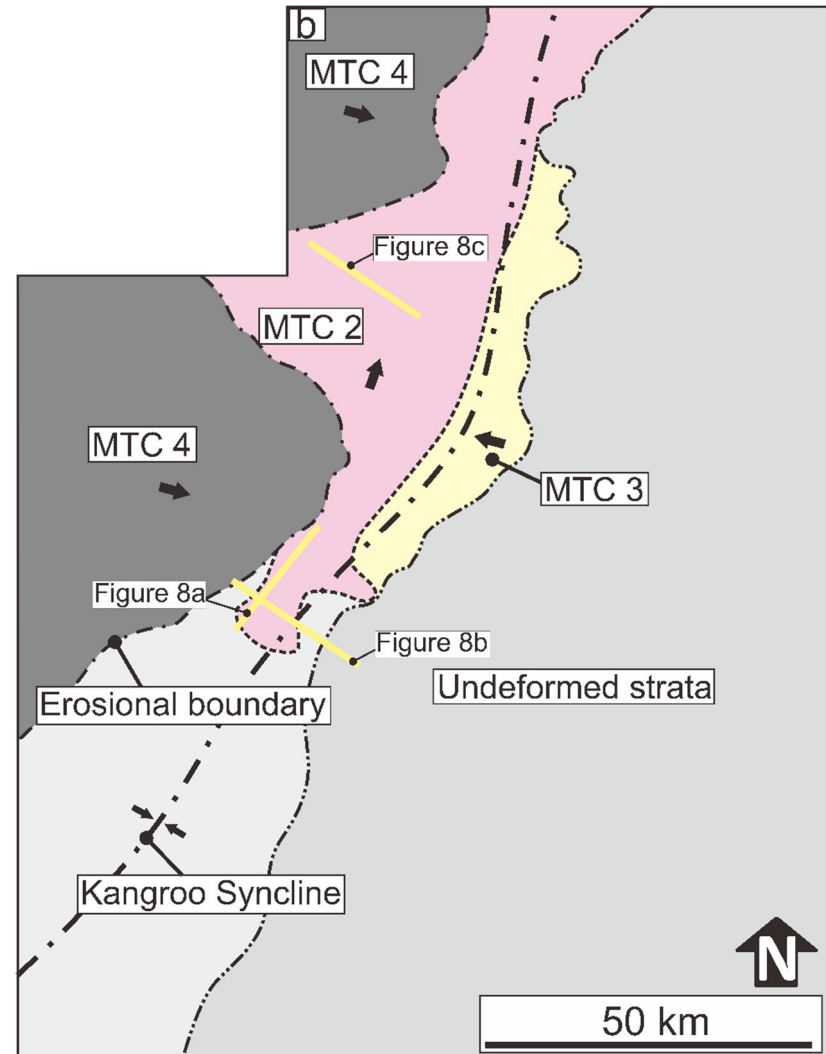
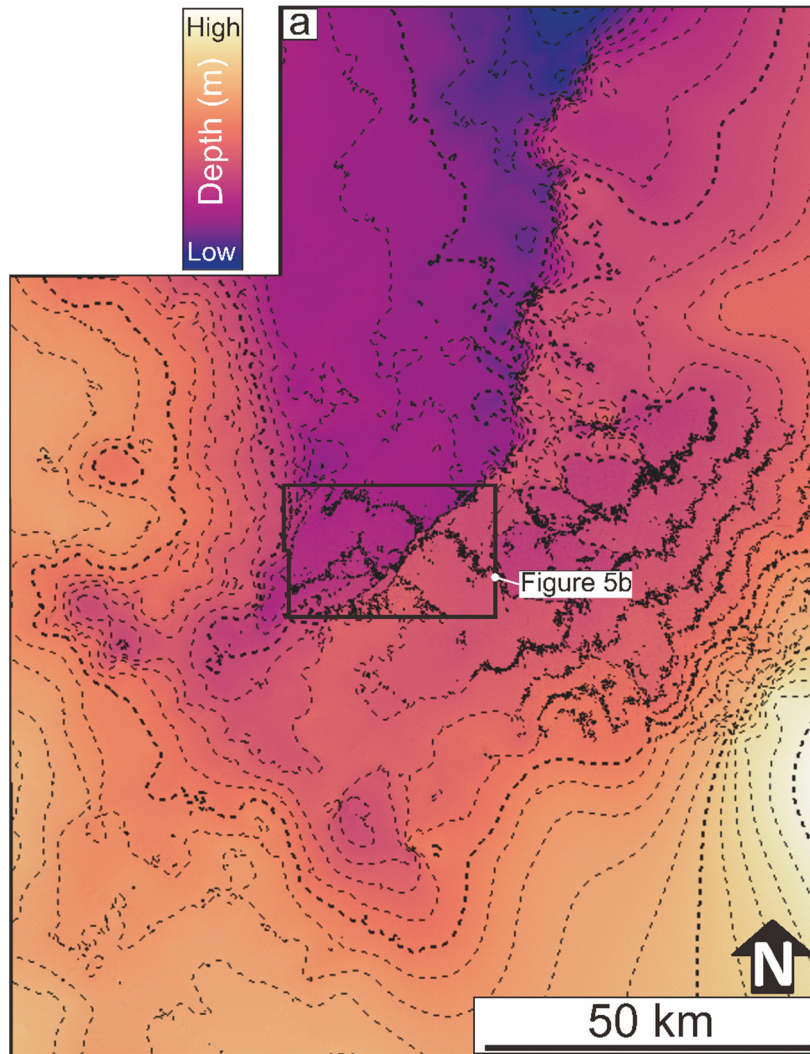


Figure 5

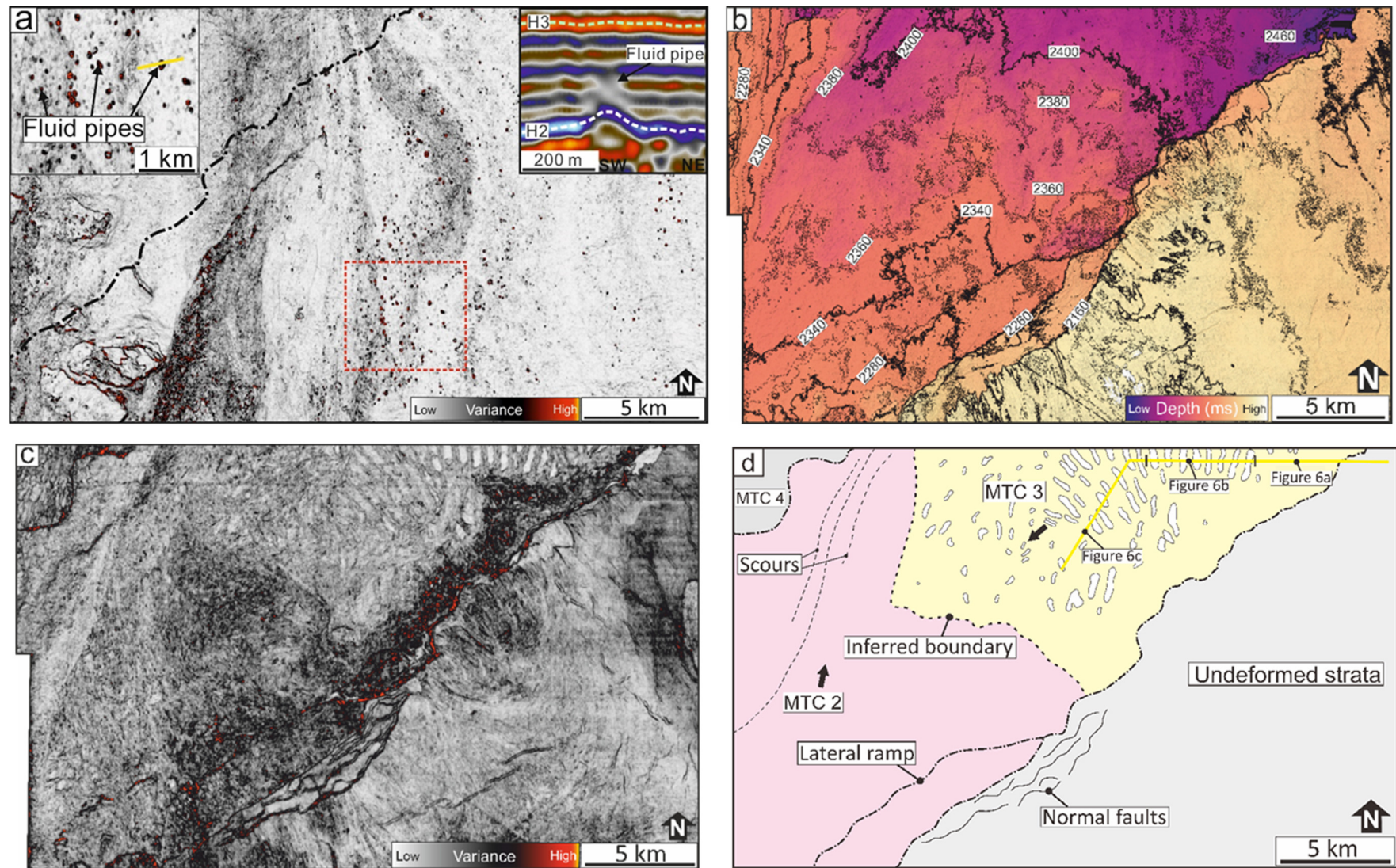




Figure 6

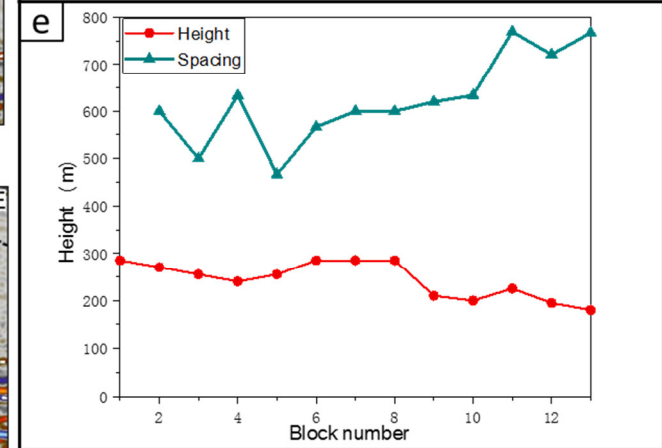
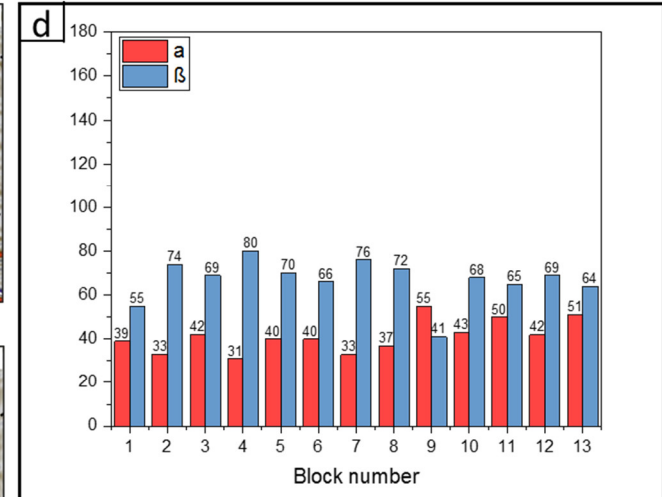
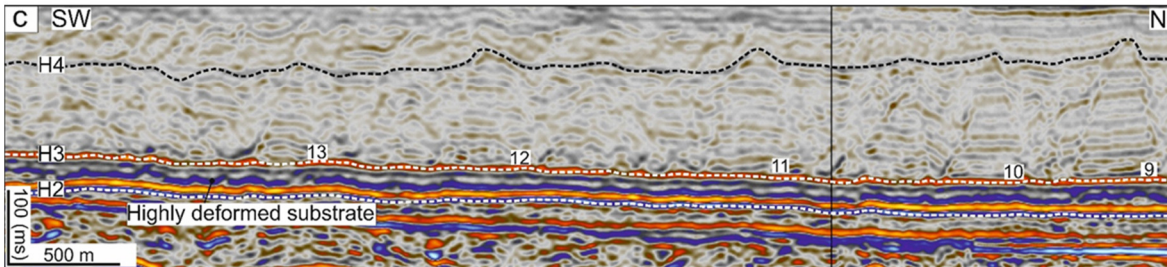
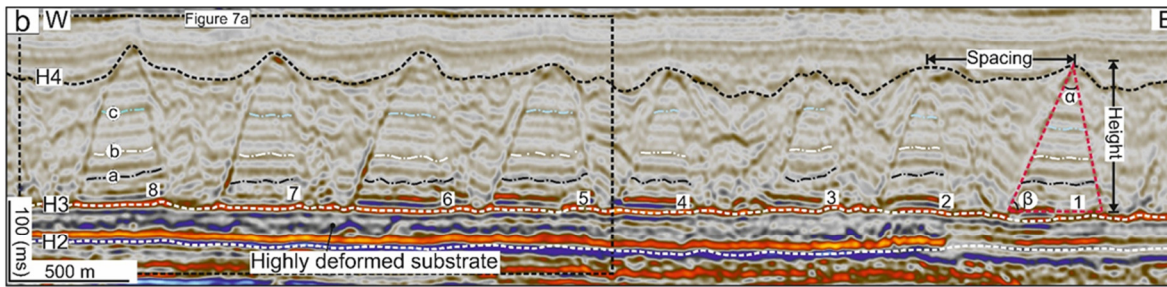
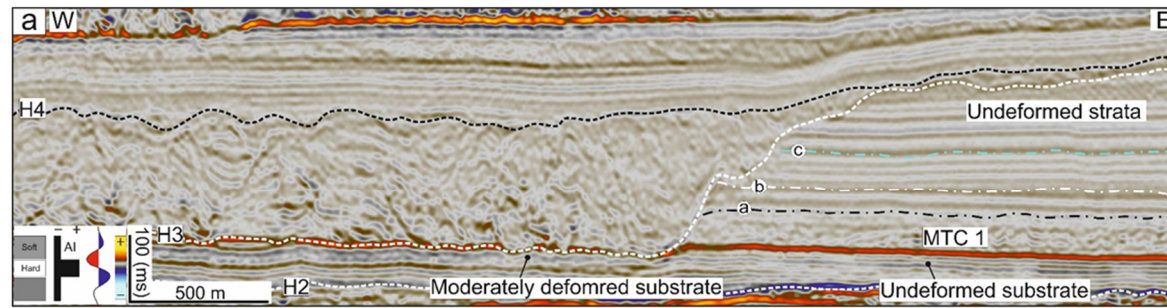


Figure 7

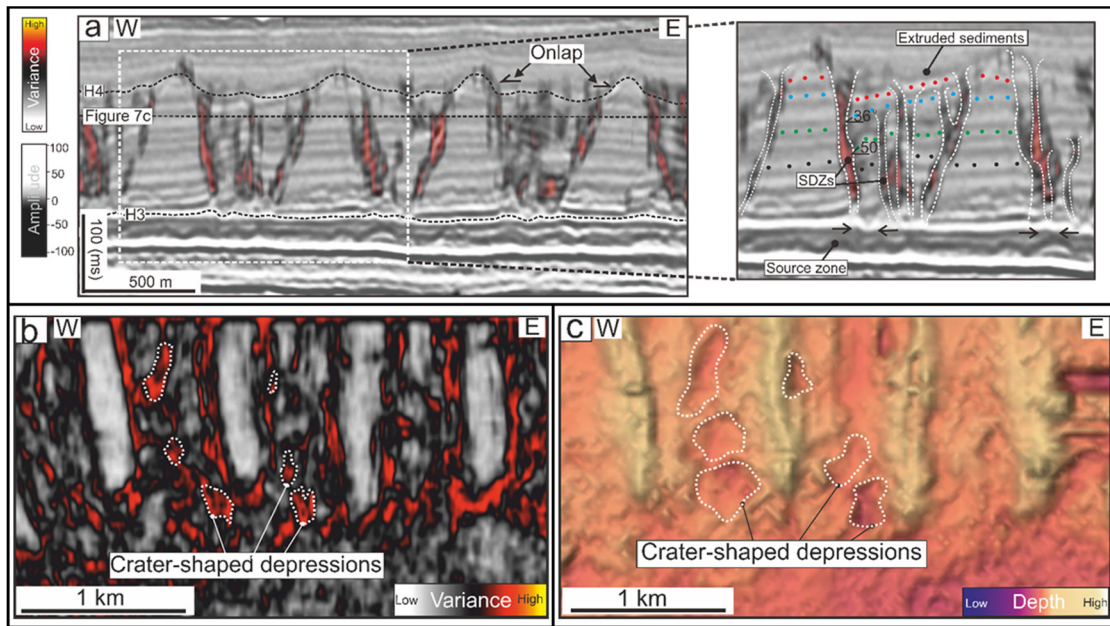




Figure 8

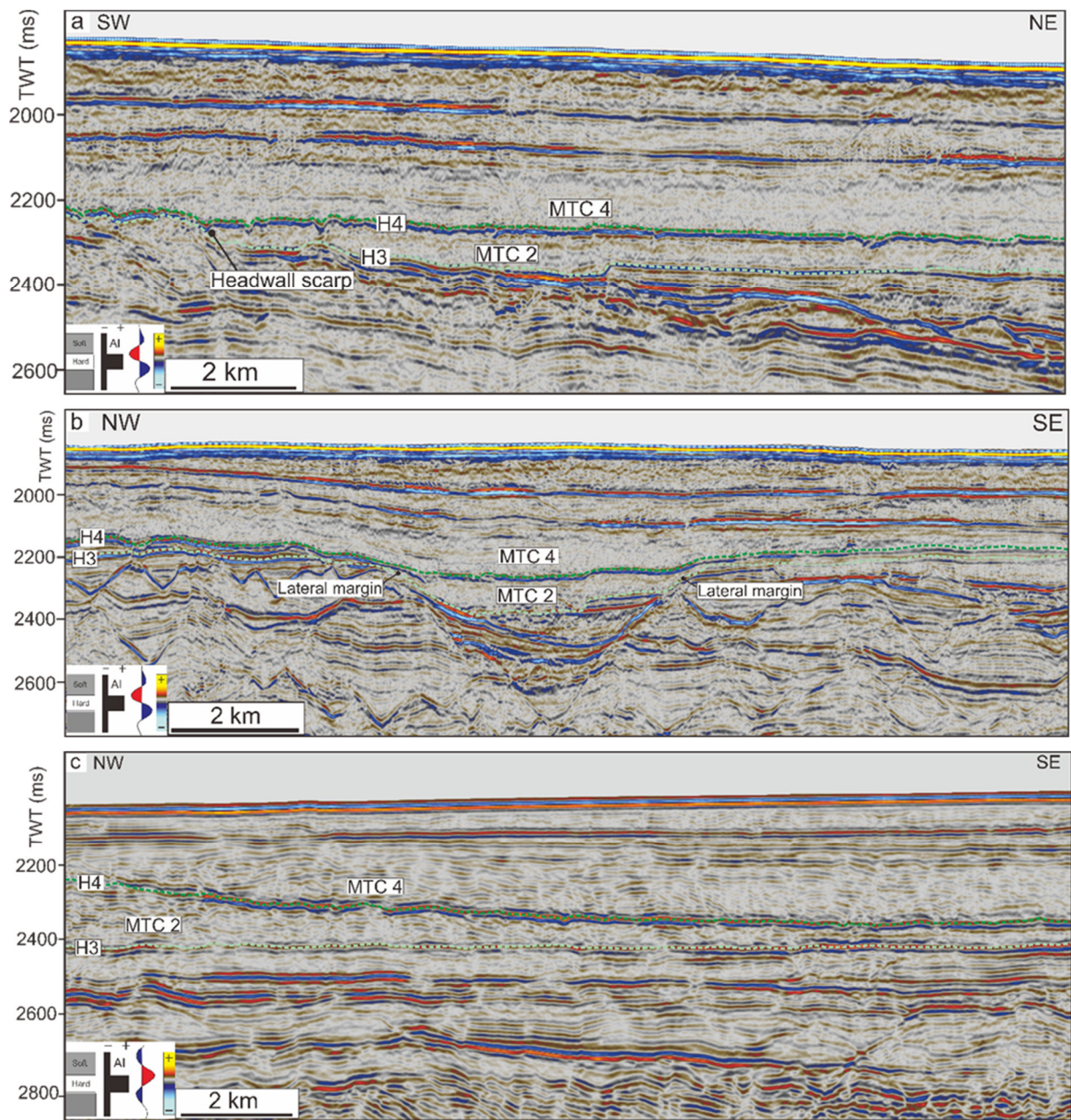




Figure 9

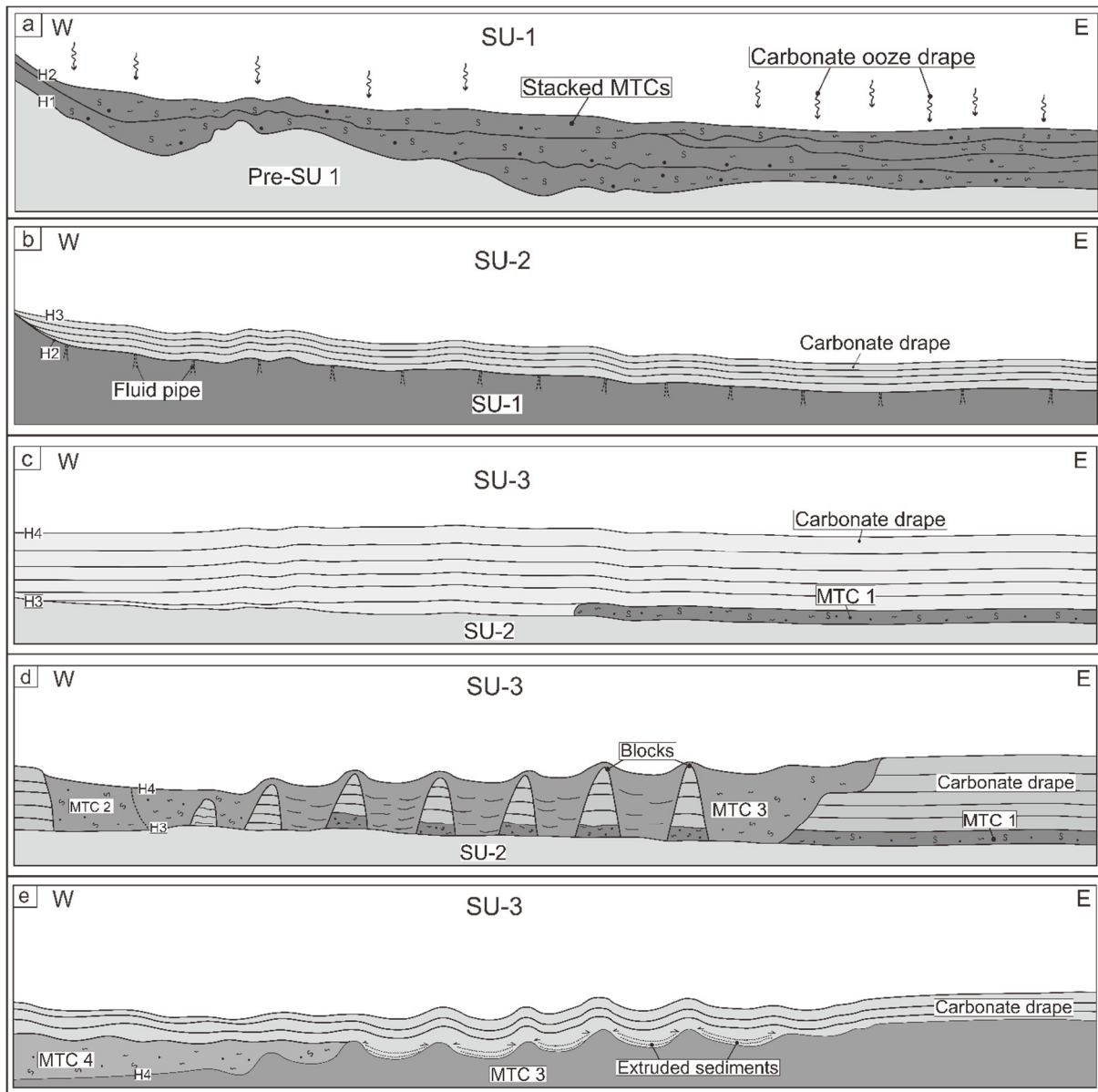


Figure 10

